

As a service to readers of *fib* Bulletin 39, which was printed in black & white, figures that were available as colour image files have been included in this PDF file.



Fig. 1-1: The Rion – Antirion bridge.

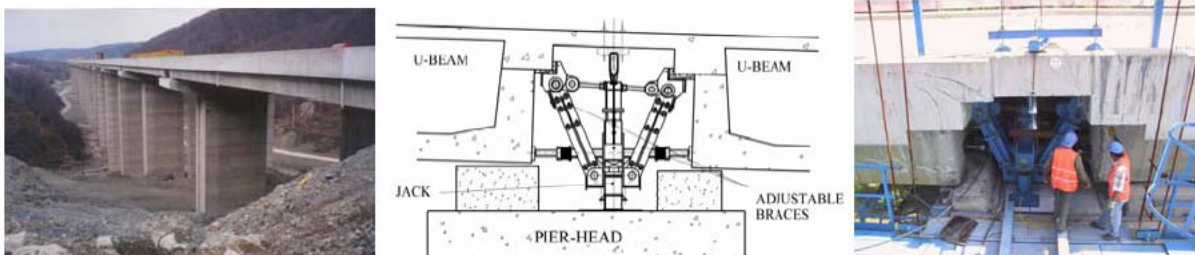


Fig. 1-2: The Bolu Viaduct, design and operation for repositioning the superstructure



Fig. 4-2: The Votonosi Bridge near Metsovo (NW Greece); the superstructure consists of a post-tensioned single cell box girder (common in modern bridges), and its 230m central span, is the longest span so far in balanced cantilever construction in Greece (Courtesy of A. Kappos).



Fig. 4-7: The G2 bridge near Kavala (NE Greece); the superstructure consists of precast post-tensioned beams connected through a cast in situ top slab (typical of older construction) (Courtesy of A. Kappos).



Fig. 4-9: Precast segmental elements for the construction of the San Francisco-Oakland Bay Bridge Skyway Structure (Courtesy of F. Seible)



Fig. 4-10: Example of use of the use of precast I-girders on a highway bridge-widening project in California (Courtesy of J. Restrepo)



Fig. 4-12: Use of a 'pre-shaft' to increase the pier length in an Egnatia bridge (Metsovitikos)



Fig. 5-16: View of the Antirion access viaduct during construction (see pile cap above ground surface)

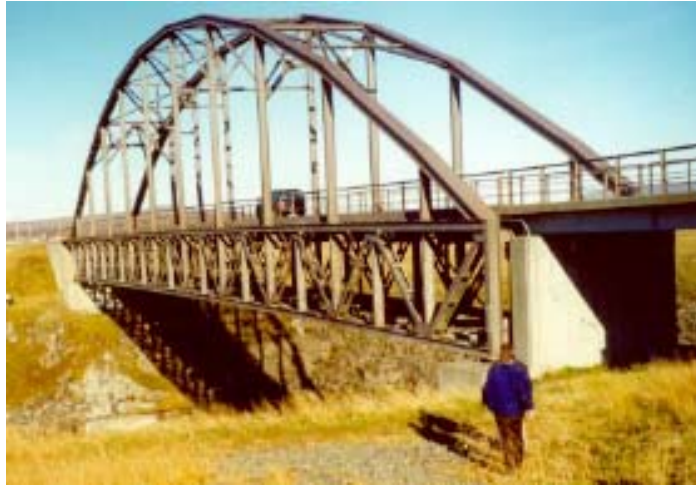


Fig. 6-5: The Thjorsa bridge in the South Iceland Lowlands (mceer.buffalo.edu).

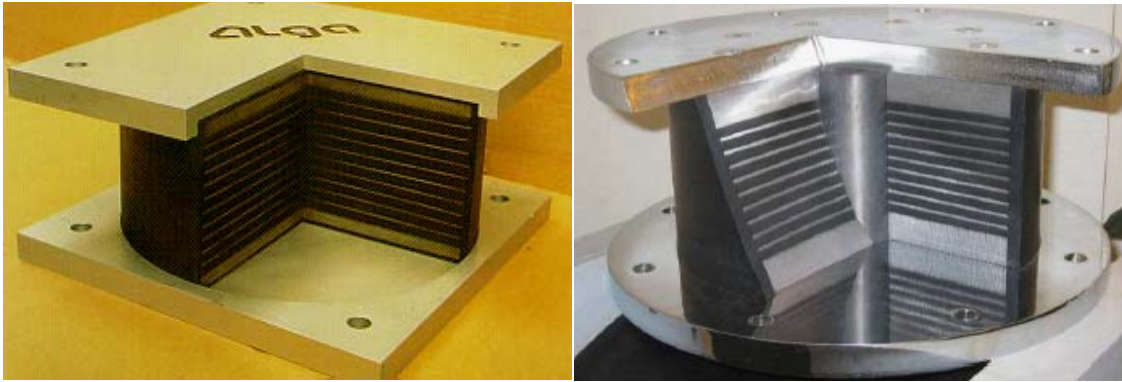


Fig. 6-8: Section of a Laminated (left) and Lead (right) Rubber Bearings.



Fig. 6-18: C-shaped Device (left) and EDU Device (right).

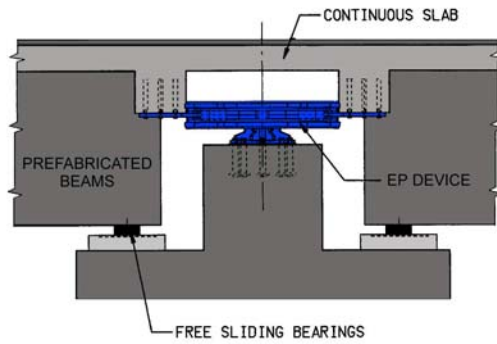


Fig. 6-19: View of the Bolu Viaduct (Priestley and Calvi, 2003) (left) and detail of the pier top (Marioni, ALGA S.p.A.) (right).

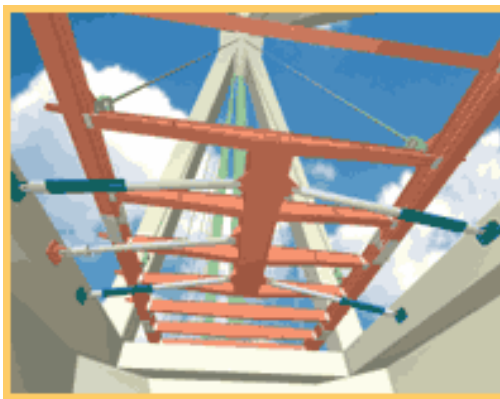


Fig. 6-25: Representation of the viscous damper units in the Rion-Antirion bridge (<http://www.gefyra.gr>) (left), example of viscous dampers application to a bridge located at Yen-Chou in Taiwan (Hwang and Tseng, 2005) (right).

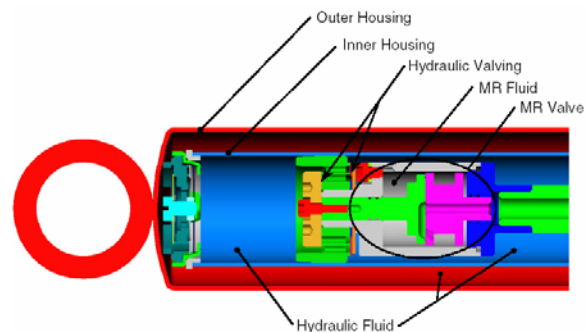
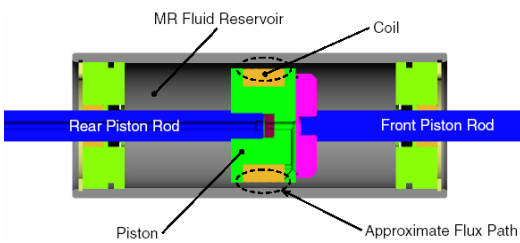


Fig. 6-33: Double-ended MR damper (left) and MR piloted hydraulic damper (right).



Fig. 6-34: ER Dampers: linear (left) and rotating (right) working schemes (Marioni, 2002).



Fig. 8-1: Wushi Bridge - fault movement between piers 2 and 3



Fig. 8-2: Wushi Bridge - span collapse due to longitudinal movement at pier P2N



Fig. 8-3: Wushi Bridge - shear failure of pier P2S



Fig. 8-4: Wushi Bridge - settlement and shear cracks at pier P3N



Fig. 8-5: Bolu Viaduct - view from abutment S2



Fig. 8-7: Bolu Viaduct - failure of an EDU



Fig. 8-8: Bolu Viaduct - unseating of beam end at pier cap



Fig. 8-13: Extended seating frame



Fig. 8-14: Extended seating frame



Fig. 8-15: Abutment with extended seating length and special bearings



Fig. 8-16: Piers with extended seating length and special bearings



Fig. 8-17: Steel bridge and in-situ concrete bridges.



Fig. 9-10: Road system of Shelby County [Werner (2004)]

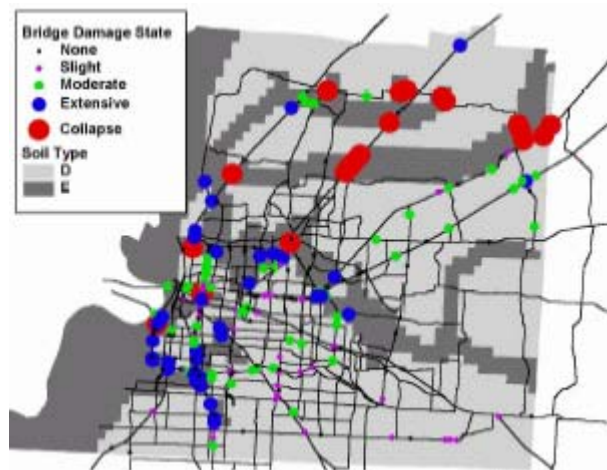


Fig. 9-12: State of the bridges in the road system of Shelby County [Werner (2000)]



Figure 10-1: Span collapses at the Golden State-Antelope Valley interchange collectors during the 1971 San Fernando (left) and the 1994 Northridge (right) earthquakes (courtesy of USGS).



Fig. 10-2: Punching of piles through the road bed of the State Route 1, Watsonville area, span during the 1989 Loma Prieta earthquake (after NISEE, 2000).



Fig. 10-3: Pounding damage: between adjacent spans at the Interstate-5 at Santa Clara River in Los Angeles County during the 1994 Northridge earthquake (left) and at the abutment of a bridge near Nishinomiya Port in the 1995 Kobe earthquake (after NISEE, 2000).



Fig. 10-4: Confinement failure at bridge pier top during the 1994 Northridge earthquake (after NISEE, 2000).



Fig. 10-5: Flexural failure above column base of columns of the Hanshin expressway, due to premature termination of longitudinal reinforcement and inadequate confinement in the 1995 Kobe earthquake (courtesy of Kawashima).



Fig. 10-6: Shear failure within (left) and outside (right) the plastic hinge region in San Fernando Mission Blvd-Gothic Avenue Bridge and I-10 Freeway at Venice Blvd, respectively, during the 1994 Northridge earthquake (after NISEE, 2000).



Fig. 10-7: Different shear damage patterns for RC piers at the under-crossing of the Santa-Monica Interstate during the 1994 Northridge earthquake: Piers # 5 with inadequate detailing for plastic hinge (left), Piers # 6 with symmetric buckling (middle) and Pier # 8 with typical shear failure (right) (after Broderick et al., 1994).



Fig. 10-8: Sliding shear at top columns of the Cypress viaduct in the 1989 Loma Prieta earthquake (after NISEE, 2000).



Fig. 10-22: Typical European viaduct.

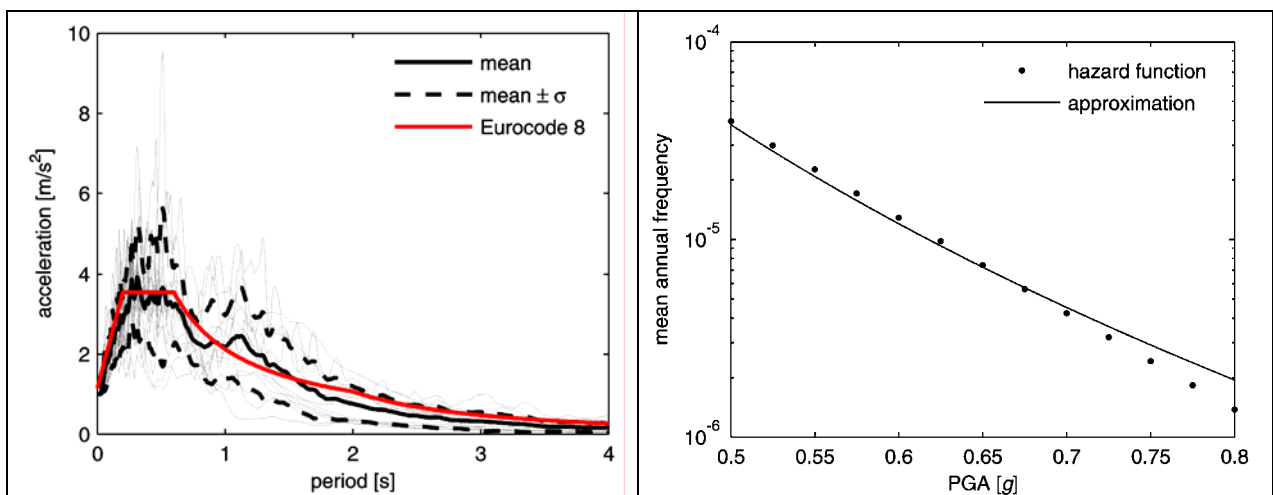


Fig. 10-23: Elastic spectra (left) and hazard function (right).

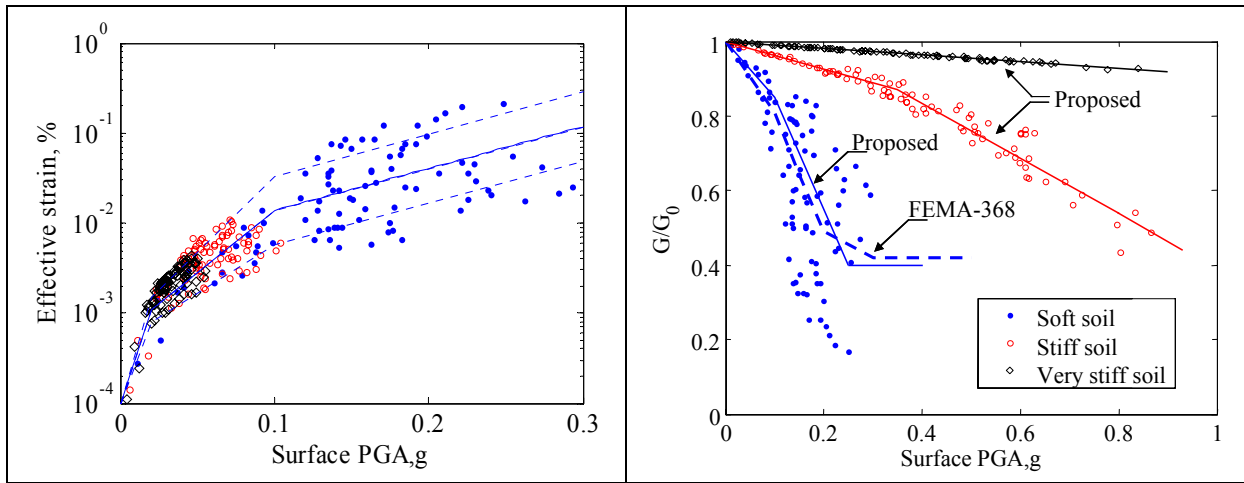


Fig. 10-25: Surface PGA and effective strain of the soft soil deposit (left) and surface PGA versus G/G_0 (right).

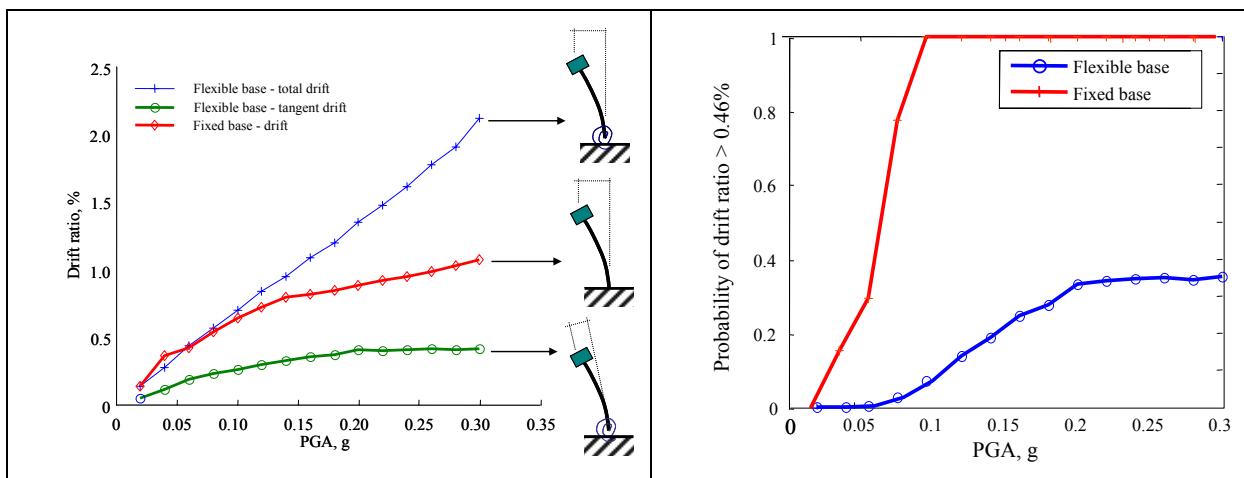


Fig. 10-26: Drifts of the SDOF system with and without SSI effects (left) and fragility curves of the SDOF (right).



Fig. 11-2: Steel jacket retrofit of columns: (a) Los Angeles, and (b) San Francisco



Fig. 11-3: Steel jacket retrofit at Metropolitan Expressway



Fig. 11-4: Steel jacket retrofit at Hanshin Expressway in 1989, which was effective during the 1995 Kobe earthquake



Fig. 11-9: Test models (9m tall and 2.5m x 2.5m section) for steel jacketing with controlled enhancement of flexural capacity



Fig. 11-12: Steel jacket retrofit for frame piers, Metropolitan Expressway, Japan

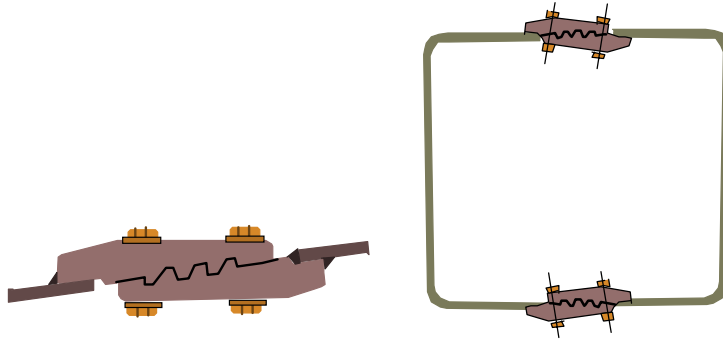


Fig. 11-13: Engagement joint (Courtesy of JR Research Institute)



Fig. 11-14: Effective use of engagement joint for retrofit at a railway viaduct (JR Research Institute)

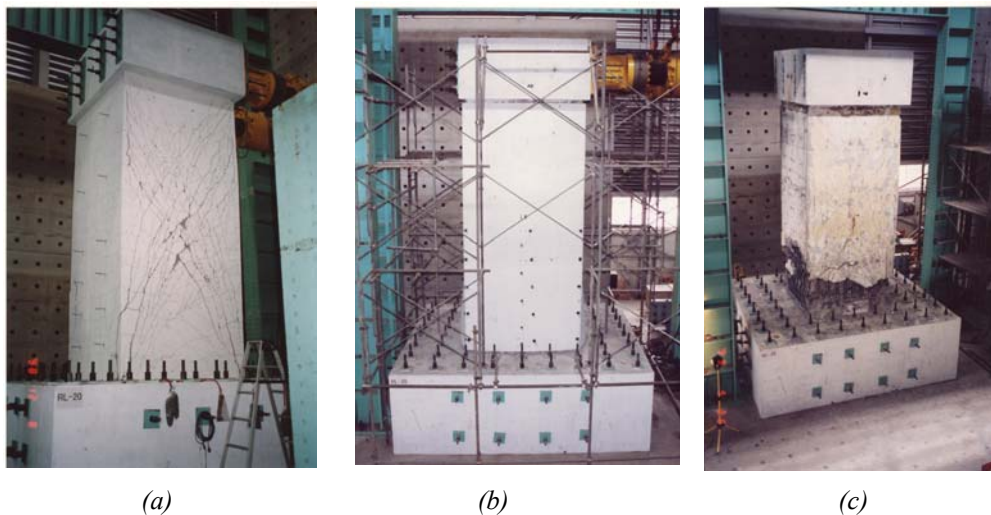


Fig. 11-15: Steel jacket repair and retrofit for shear; (a) shear failure after loaded, (b) repaired by steel jacketing, and (c) flexural failure of retrofitted column (after steel jacket was removed) [Iwata et al. (2001)]



(a)

(b)

Fig. 11-20: Cyclic loading test on the retrofit of wall pier by steel jacket covered by reinforced concrete jacket with cross aramid fiber reinforced plastics rods: (a) As-built pier, and (b) Pier retrofitted using cross aramid fiber reinforced plastics rods [Tamaoki et al. (1996)]



(a)



(b)



(c)

Fig. 11-21: Retrofit using cross aramid fiber reinforced plastics rods to wall piers: steel jacketing, (b) set of cross aramid fiber reinforced plastics rods, and (c) after retrofitted (courtesy of Sumitomo Mitsui Construction)

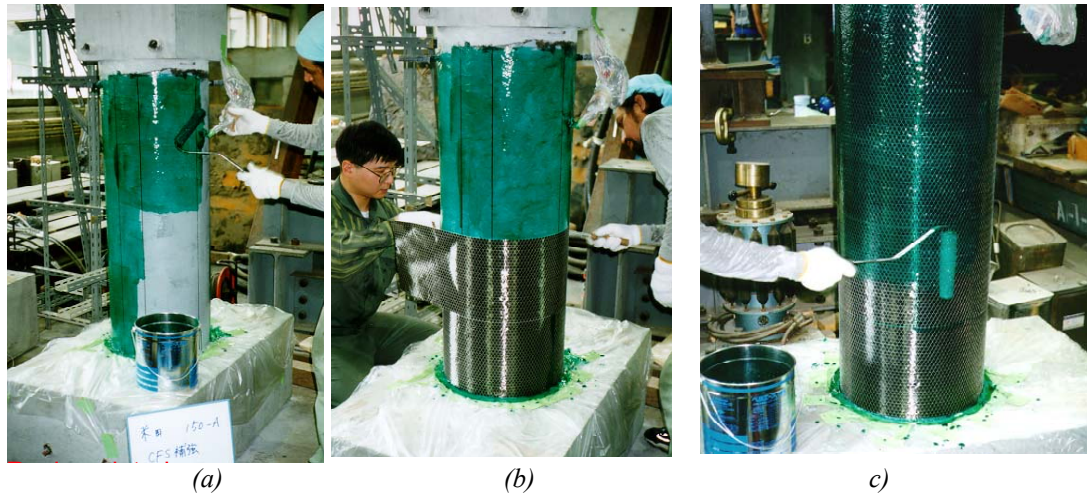


Fig. 11-23: Wrapping of carbon fiber sheet: (a) pasting glue, (b) wrapping the first layer, and (c) bonding on the first layer



Fig. 11-27: Carbon fiber sheet jacketing of hollow reinforced concrete columns, Sakawa-gawa bridge, Tomei expressway; (a) Retrofitted east- and west-bound bridge, and (b) Wrapping of carbon fiber sheets [Ogata et al. (1999), Osada et al. (1999)]



Fig. 11-30: Aramid fiber reinforced plastics jacketing for a railway viaduct [courtesy of JR Research Institute]



Fig. 11-31: Piers retrofitted by aramid fiber sheet [Kato et al. (2001)]

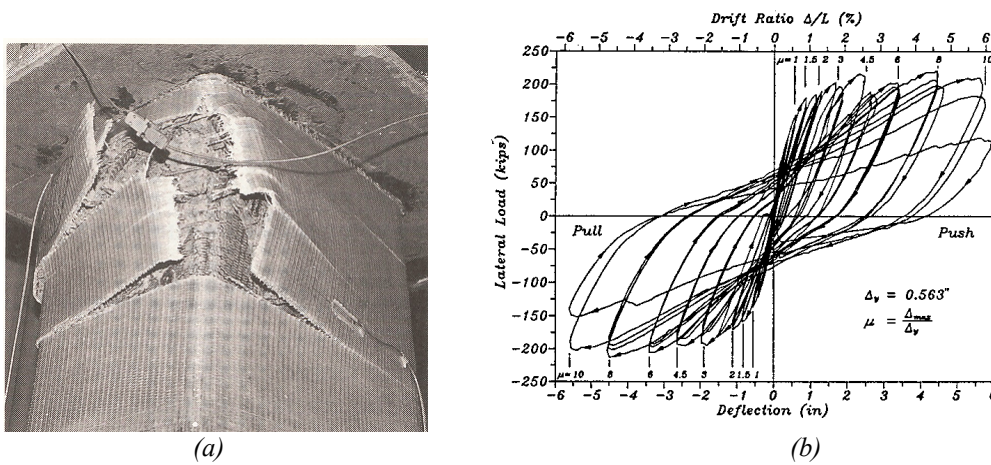


Fig. 11-33: Rectangular column with glass fiber-epoxy rectangular jacket: (a) failure by jacket fracture, (b) lateral force-displacement response [Priestley, Seible and Calvi (1996)]



Fig. 11-34: Glass fiber jacking (courtesy of JR Research Institute)



Fig. 11-35: Precast concrete segment jacket [courtesy of PS Concrete]



Fig. 11-36: On-site loading test on the effectiveness of PC segment jacketing



(a) before retrofit

(b) after retrofit

Fig. 11-37: Columns retrofitted by PC segment jacket: (a) as-built and (b) after retrofit (courtesy of Kawada Construction)



(a)



(b)



(c)



(d)

Fig. 11-42: Retrofit of wall pier by PC segment jacket: (a) as-built pier, (b) set of a precast segment using temporary joints, (c) anchor bolt for confinement (up) and anchor bolt for footing (bottom), and (d) after retrofitted (courtesy of Maeda Construction)



(a)



(b)

Fig. 11-43: Collapse of Cypress viaduct (Courtesy of Caltrans)

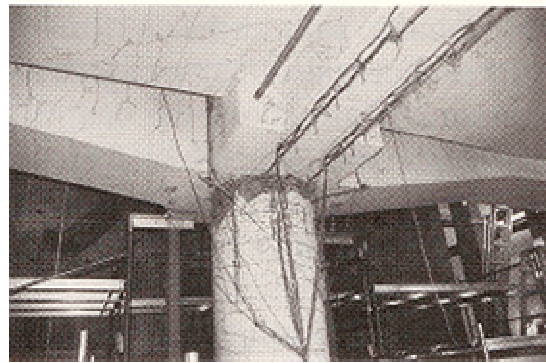
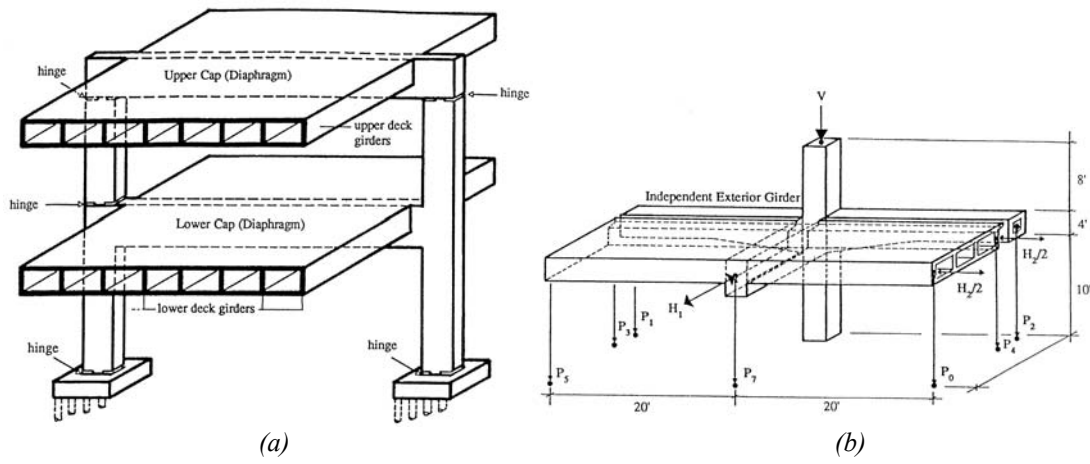


Fig. 11-46: Retrofit of San Francisco double-deck viaducts using edge link beams: (a) as-built viaduct, (b) proof test model, (c) proof test, (d) column damage in the proof test, (d) retrofit, and (e) edge beams [(a)-(d): Priestley, Seible and Calvi (1996)]



(a)



(b)



(c)

Fig. 11-52: Footing retrofit: (a) extension of footing and new piles (California, USA), (b) extension of footing and new piles (Japan), and (c) Overlay of footing (Japan)

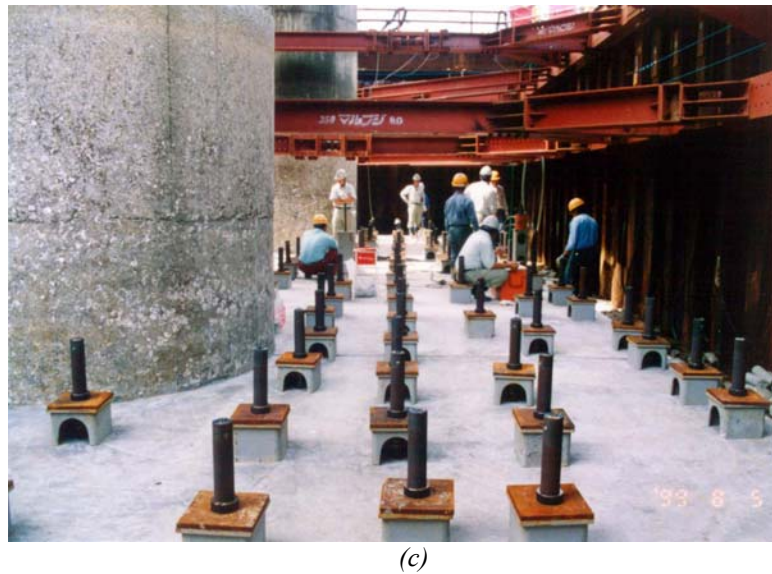


Fig.11-54: Retrofit of a footing using aramid fiber reinforced plastic rods: (a) as-built bridge, (b) aramid fiber reinforced plastic rods, and (c) aramid fiber reinforced plastic rods installed in the footing in the vertical direction [courtesy of Sumitomo Mitsui Construction]

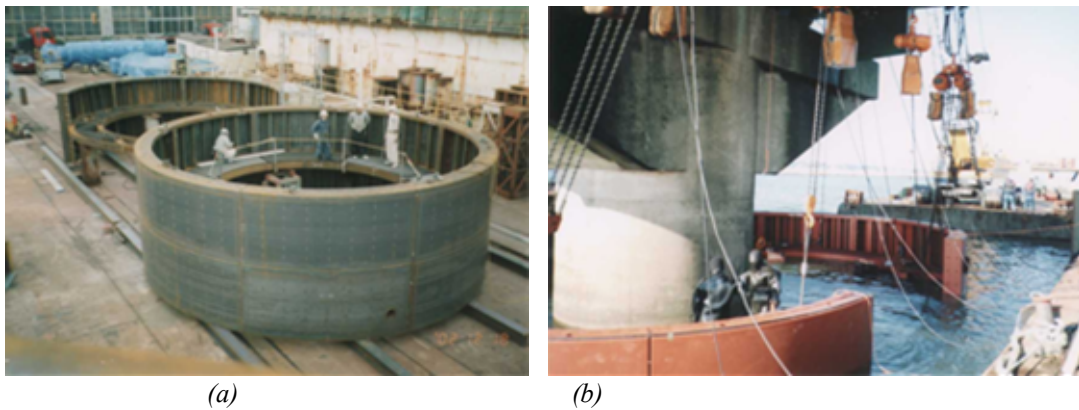


Fig. 11-55: Implementation of steel segment dry-up method: (a) assembling test, and (b) assembling the segments around the foundation [courtesy of Obayashi Construction]



(a)



(b)

Fig. 11-57: Micro piles for retrofit of foundations: (a) drilling and (b) micro piles after installation [Nishitani et al. (2002)]



Fig. 11-61: Damage of intermediate joint due to pounding (1994 Northridge earthquake)



(a)



(b)

Fig. 11-62: Installation of cable restrainers (courtesy of California Department of Transportation)



Fig. 11-67: Seismic retrofit using isolation: (a) installation of lead rubber bearings and sliding bearings, and (b) after retrofit (courtesy of Japan Highway Public Corporation)



Fig. 11-68: Connection of decks and retrofit: (a) removal of existing steel bearings, and (b) set of new lead rubber bearing (courtesy of Hanshin Expressway Public Corporation)



Fig. 11-71: Shake table test for the effectiveness of compression damper brace [Yoshida et al. (2005)]



Fig. 11-73: Viaduct retrofitted using compression brace damper [Yoshida et al. (2005)]



(a)



(b)



(c)



(d)

Fig. 11-76: Retrofit of a simply supported bridge using pipe arches: (a) before retrofit, (b) after retrofit, (c) pipe arches, and (d) connection between arches and a foundation [Mizuta and Hashimoto (2001)]